



The influence of wind veer on fatigue loading for large floating wind turbines with flexible drivetrains

Veronica Liverud Krathe¹, Jason Jonkman², and Erin E. Bachynski-Polić¹

¹Department of Marine Technology, Norwegian University of Science and Technology (NTNU), Trondheim, Norway

²National Renewable Energy Laboratory (NREL), Golden, Colorado, United States

Correspondence: Veronica Liverud Krathe (veronica.l.krathe@ntnu.no)

Abstract. To reduce cost, offshore wind turbines are expected to be designed with significantly increased rotor diameters. Larger turbines become more flexible and span a larger portion of the atmospheric boundary layer. With these changes, the validity of traditional modeling assumptions should be investigated. This work challenges two common assumptions: 1) that the drivetrain can be considered rigid (except in torsion) and does not couple with the rotor and tower and 2) that wind directional change with height (veer) does not greatly influence the fatigue damage in the tower, blades and drivetrain.

Two large floating wind turbines are considered: the International Energy Agency (IEA) 15 MW (Gaertner et al., 2020) reference turbine with the University of Maine VoltturnUS-S platform (Allen et al., 2020) and the IEA Wind 22 MW reference turbine (Zahle et al., 2024a). Both are direct-drive generator turbines supported by semisubmersible platforms. Aero-hydro-servo-elastic simulations are performed using OpenFAST, with drivetrain bending flexibility and main bearing response implemented in the coupled analysis. The turbines are subjected to a set of load cases at below-, near- and above-rated mean wind speeds, assembled based on NORA3 hourly wind and wave hindcast data (Haakenstad et al., 2021) for Utsira Nord off the coast of Norway (Cheynet et al., 2023, 2024). Within each load case, conditions with and without veer are simulated to evaluate the influence of veer on damage equivalent loads (DELs) of the turbine tower, blades and main bearings. Further, these load cases are applied to evaluate the influence of drivetrain flexibility on global turbine response.

The results indicate that, depending on the veer gradient, operating regime and turbine size, veer can be very important for DELs of the tower top and blade root and for the fluctuations of the main bearing radial loads. Moreover, drivetrain flexibility is found to influence global DELs, especially for the largest turbine. Comparing flexible and rigid drivetrains, the tower-top fore-aft and torsional damage equivalent moments of the 22 MW turbine are reduced by more than 20 % at near rated wind speeds. For the same turbine in below-rated wind speeds, the blade root flapwise DELs are reduced by up to 6 %.

1 Introduction

Offshore wind turbines are expected to reach rated capacities of 15 MW and beyond (IRENA, 2019). With increasing turbine size, the applicability of current modeling approaches becomes more uncertain. Mechanisms that have been neglected in the design of smaller turbines may play an important role for larger wind turbines. Increased structural flexibility is one feature that introduces new demands on state-of-the-art analysis tools. Another challenge emerges from the rotor extending deeper into, or



25 even beyond, the atmospheric boundary layer (ABL), so that previous assumptions related to the wind profile and wind field can be questioned. In this work, both of these topics are investigated.

Based on the assumption of a relatively rigid drivetrain, main bearing response has traditionally been obtained by two separate analyses. First, a global analysis, with the drivetrain represented by a torsional spring and damper, outputs shaft loads. These shaft loads are then combined with either analytical calculations or a detailed local model of the drivetrain to obtain main bearing loads. Analytical calculations are fast but complex to derive for bearings that have off-diagonal or moment-carrying stiffness terms. Local models are accurate but computationally expensive and time-consuming to develop. Additionally, the decoupling of drivetrain flexibility from global turbine response becomes questionable as turbines become larger and more flexible (Torsvik, 2020). For instance, Wang et al. (2021) found non-torsional modes of the drivetrain with lower natural frequencies than the torsional mode when considering a fully coupled drivetrain-turbine model.

35 In design, the wind profile has typically been assumed as sheared (mean speed varying with height) but without variation of mean wind direction with height. A common definition of wind "veer" is the clockwise rotation of the mean wind direction with height, while "backing" refers to winds rotating counterclockwise with height (Lundquist, 2022). Veer is a phenomenon often associated with stable boundary layers (Stull, 1988). Shu et al. (2020) found the largest veer angles for neutrally stratified boundary layers using lidar measurements off the coast of Hong Kong. Wind veer often stems from the influence of frictional forces on the force balance. The frictional forces are present in the ABL, diminish with height, and are not present in the troposphere. Veer can also be a result of inertial oscillation in the ABL or horizontal temperature gradients (Lundquist, 2022). Offshore measurements near Martha's Vineyard collected over 13 months showed that strong wind veer often occurred, especially in the spring and summer and with low wind speeds (average values of up to 0.1° m^{-1} and extreme values above 0.3° m^{-1}) (Bodini et al., 2019, 2020). Veer and backing occurred 70 % and 30 % of the time, respectively. A similar ratio of backing to veer was found by Marini et al. (2025) based on 12 months of lidar measurements in Belgian waters (excluding June and August) and with occurrences of high veer gradients above 0.3° m^{-1} . Shu et al. (2020) also found decreasing veer gradient with increasing wind speed.

Two studies investigated the sensitivity of a 5 MW wind turbine to various modeling parameters; Robertson et al. (2019) considered an onshore variant while Wiley et al. (2023) considered the same turbine atop a semisubmersible. Robertson et al. (2019) observed that turbine fatigue loads (tower, blade-root and main shaft bending moments) were less influenced by veer than by turbulence and shear. Similarly, Wiley et al. (2023) found low sensitivity of fatigue-proxy loads to veer compared to wind velocity standard deviation, turbulence coherence and the wave conditions. On the other hand, Hart et al. (2022) found that veer significantly influenced the main bearing radial load fluctuations, more so than the other deterministic effects they evaluated (shear, yaw offset, mean wind speed), for a 5 MW onshore turbine. They used a simplified load response model and deterministic wind fields. Larger veer led to larger fluctuations, while negative veer (backing) of the same magnitude led to a smaller increase in radial load fluctuations. Applying similarity scaling to 7.5 MW and 10 MW turbines, veer was seen to scale more than cubically with rotor radius. To the authors' knowledge, there are no studies on the influence of veer on turbine loads for turbines larger than 10 MW, and the IEC 61400-1 wind turbine design standard (IEC, 2019) does not mention veer, even



though it is an inherent characteristic of the wind field. A rotor spanning 200 to 300 m can potentially sample a large variation
60 of wind directions, and it is important to understand the effects of veer on turbine loads.

This paper addresses the influence of increased drivetrain flexibility and wind veer on damage-equivalent loads (DELs) in
the tower, blade root and main bearings for two floating turbines. A coupled drivetrain-turbine model was built in OpenFAST.
This modeling approach was previously verified against a multibody model (Krathe et al., 2025a) and applied in investigations
of wake effects on main bearings (Krathe et al., 2025b). The model includes a flexible bedplate and shaft, both represented by
65 linear beams, and flexible main bearings are included by means of constant stiffness matrices. The model enables investigation
of the influence of drivetrain flexibility on the turbine response. It also allows for inclusion of main bearing off-diagonal
stiffness terms and direct extraction of main bearing response from global analyses. With regards to veer, reanalysis data
from NORA3 (Haakenstad et al., 2021; Cheynet et al., 2024, 2023) were applied to estimate appropriate veer gradients and
accompanying turbulence intensities, shear profiles and wave conditions for four different mean wind speeds for the Utsira
70 Nord site, designated for floating wind farms.

Section 2.1 describes the reference wind turbines and the flexible drivetrain model. Section 2.2 presents the load cases and
the derivation of the environmental conditions. Section 2.3 explains the calculation of DELs. Section 3 presents and discusses
the results, including modal analysis of the turbines with and without flexible drivetrains (Sect. 3.1), influence of drivetrain
flexibility on turbine response (Sect. 3.2), and the DELs of the tower, blades and main bearings subjected to various wind fields
75 (Sect. 3.3). Conclusions are summarized in Section 4.

2 Methodology

2.1 Wind turbine model

2.1.1 Base cases and numerical setup

Two floating reference turbines, the International Energy Agency (IEA) 15 MW (Gaertner et al., 2020; Allen et al., 2020) and
80 the IEA 22 MW turbine (Zahle et al., 2024a), were considered in this work. Both have direct-drive generators and are supported
by semisubmersible floating platforms with one centered column, three radially spaced columns and three catenary mooring
lines. The main properties of the turbines are listed in Table 1, and the drivetrain and floater of the IEA 15 MW turbine are
shown in Fig. 1.

The turbines were modeled in the aero-hydro-servo-elastic code OpenFAST (Jonkman et al., 2024). A ROSCO controller (Ab-
85 bas et al., 2024) was applied for each turbine. For such large rotors, it is generally recommended to account for large deflections
in OpenFAST by modeling the blades using the geometrically exact beam theory in the module BeamDyn. Unfortunately, it
was not computationally feasible to combine BeamDyn and the drivetrain model described in Sect. 2.1.2 for the floating tur-
bines. Instead, ElastoDyn was applied, using a modal representation of the blades. Tower influence on wind speed was included
using potential flow theory with the Bak correction (Bak et al., 2001).



Table 1. Main parameters of the floating turbines

Turbine	Hub height [m]	Rotor diameter [m]	Rated wind speed [m s^{-1}]	Rated power [MW]	Rated rotor speed [rpm]	Shaft tilt angle [$^{\circ}$]	Water depth [m]
IEA 15 MW	150	240	10.59	15	7.56	6.0	200
IEA 22 MW	170	284	11	22	7.06	6.0	200

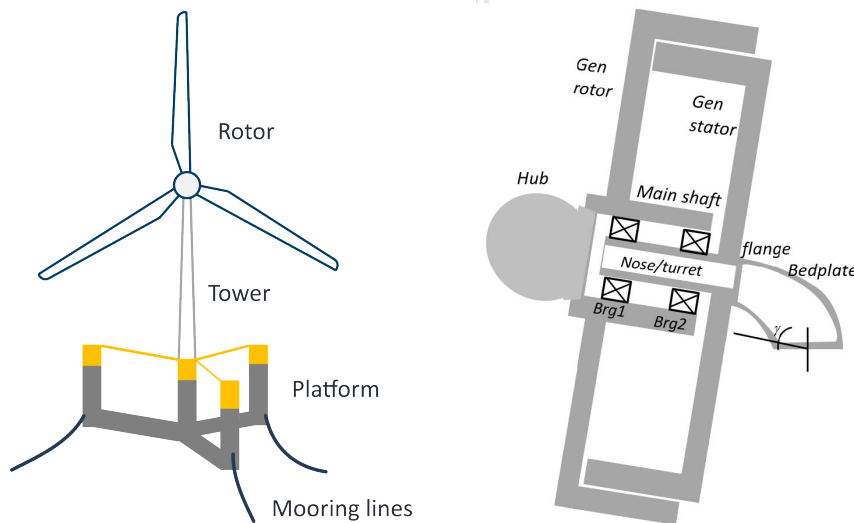


Figure 1. The IEA 15 MW reference turbine (Krathe et al., 2025b) and its direct-drive generator (Gaertner et al., 2020). The IEA 22 MW turbine has a similar design.

90 2.1.2 Drivetrain model

In this work, the two reference OpenFAST models (Barter et al., 2024; Zahle et al., 2024b) were modified to include a flexible drivetrain, modeled together with the tower in the OpenFAST linear finite element module SubDyn (NREL, 2024). This methodology was previously verified against a coupled multibody model and applied for a 10 MW geared drivetrain (Krathe et al., 2025a) and for the IEA 15 MW direct-drive turbine (Krathe et al., 2025b). In short, a flexible drivetrain was included in the coupled, global analyses. Flexible beams were applied to represent the bedplate and shaft, and constant springs represented the main bearings. Additional drivetrain mass and inertia were modeled using point masses. More details of this modeling approach can be found in the two aforementioned papers and on GitHub (Krathe, 2024). For comparison, OpenFAST models with rigid drivetrains and flexible towers were also built in SubDyn. Figure 2 presents the two versions of the global model with flexible and rigid drivetrains.

100 For the flexible drivetrain, the bedplate and shaft geometry and material properties were obtained directly from the WISDEM framework for each turbine (Barter et al., 2024; Zahle et al., 2024b). The bearings are taken as two spherical roller bearings

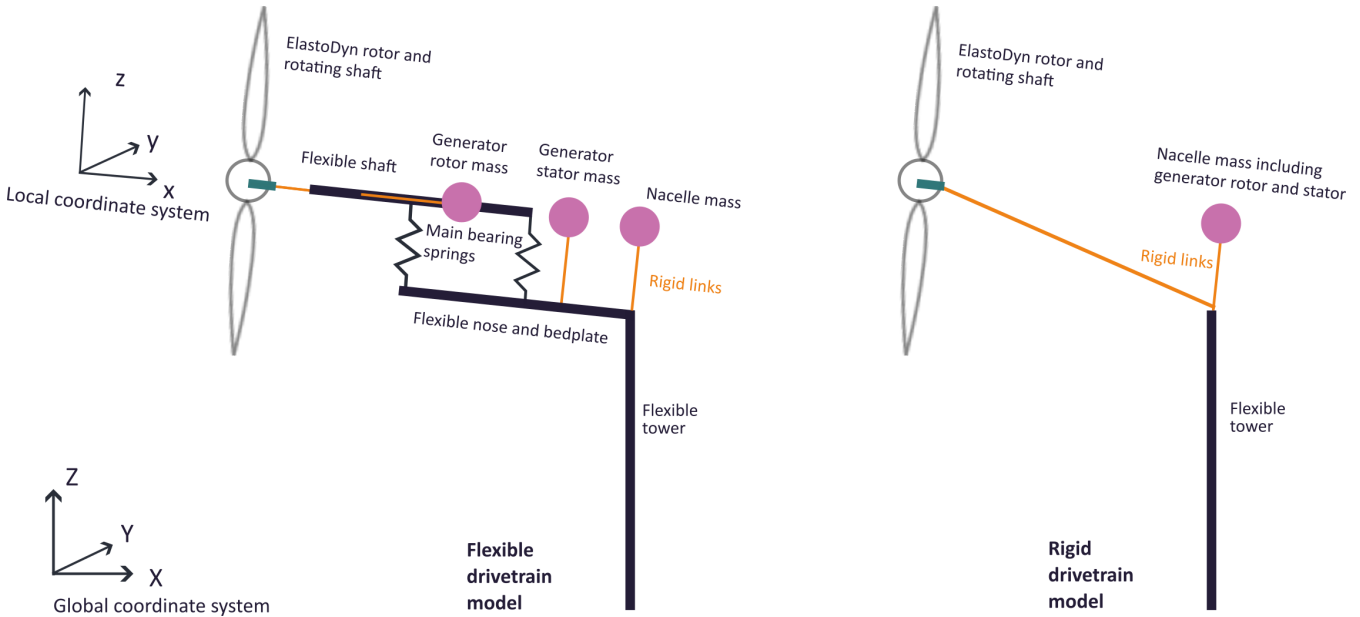


Figure 2. Flexible and rigid drivetrain models in an aero-hydro-servo-elastic simulation framework. Local and global coordinate systems, applied for the main bearings and tower response, respectively, are also presented. From Krathe et al. (2025b) with modifications.

(SRBs): an upwind non-locating SRB and a downwind locating SRB. The upwind and downwind main bearings are referred to as MB1 and MB2, respectively. The diagonals of the main bearing stiffness matrices were estimated using Schaeffler’s tool (Schaeffler, 2025) considering the force and deflection of the bearings for a number of different combinations of mean loads.

SRBs subjected to combined radial and axial loads have cross-coupling stiffness terms that are not easily estimated based on the aforementioned method. Royston and Basdogan (1998) found that these off-diagonal terms, $k_{xy} = k_{yx}$ and $k_{xz} = k_{zx}$, were typically an order of magnitude smaller than the values of k_{xx} and k_{yy} , respectively. Therefore, the cross-coupling terms were crudely estimated as $k_{xy} = \frac{0.1(k_{xx} + k_{yy})}{2}$. The estimated spring stiffnesses are summarized in Table 2. Note that the main bearing stiffness estimates differ from those presented by Krathe et al. (2025b) due to updates in estimation methodology. Note also that there are large uncertainties in the main bearing stiffness estimates, and that applying constant stiffnesses is in itself an approximation. Therefore, upper, medium and lower stiffness estimates are presented ("high", "medium" and "low"). The majority of the simulations were run with the "medium" stiffness, but in Sect. 3.2.2, the sensitivity of results to main bearing stiffness is discussed.

Table 3 documents the numerical setup in SubDyn for the different versions of the two turbine models. The IEA 22 MW turbine and IEA 15 MW turbine were run with a glue-code (OpenFAST) time step of 0.0015 s and 0.0025 s, respectively.



Table 2. Main bearing spring stiffness in local coordinates. Low (L), medium (M) and high (H) values are shown as L/M/H. The "medium" values were applied in all simulations, except for the sensitivity study presented in Sect. 3.2.2.

Bearing	k_{xx} [N m ⁻¹]	$k_{yy} = k_{zz}$ [N m ⁻¹]	$k_{xy} = k_{xz}$ [N m ⁻¹]
15 MW, MB1	0	1.04E10/ 2.09E10 / 2.75E10	0
15 MW, MB2	1.32E8/ 1.85E8 / 2.13E8	7.35E10/ 8.41E10 / 8.96E10	5.27E8/ 1.05E9 / 1.38E9
22 MW, MB1	0	2.39E10/ 3.50E10 / 3.99E10	0
22 MW, MB2	2.12E8/ 6.67E8 / 1.27E9	3.85E10/ 6.53E10 / 9.16E10	1.21E9/ 1.78E9 / 2.06E9

Table 3. SubDyn numerical setup. The glue-code (OpenFAST) time steps were set similar to the SubDyn time steps.

Parameter	IEA 15 MW	IEA 15 MW	IEA 22 MW	IEA 22 MW
	flexible drivetrain	rigid drivetrain	flexible drivetrain	rigid drivetrain
SubDyn time step [s]	0.0025	0.0025	0.0015	0.0015
No. of Craig–Bampton modes [-]	16	14	25	20
Craig–Bampton modes damping (percentage of critical) [%]	0.5	0.5	0.5	0.5
Frequency of upper retained Craig–Bampton mode [Hz]	18.0	18.7	27.4	32.4

2.2 Environmental load cases

2.2.1 Environmental data

NORA3 (Norwegian Reanalysis) (Haakenstad et al., 2021; Haakenstad and Breivik, 2022) is a wind and wave hindcast dataset for Northern Europe (Cheynet et al., 2024). It spans 1982 to 2022, has a horizontal resolution of 3 km, a temporal resolution of 1 hour, and is a downscale of the ERA5 reanalysis (Hersbach et al., 2020). Based on NORA3, Cheynet et al. (2023, 2024) generated spatially averaged data for two Norwegian offshore wind turbine locations. In this work, 1-hour median data for the deep-sea location Utsira Nord, designated for floating offshore wind farms, are applied to estimate environmental load conditions. Data are available at heights of 10, 20, 50, 100, 150, 250, 500 and 750 m.

The veer gradient was calculated using an expression for bulk veer (Murphy et al., 2020):

$$\beta = \frac{\theta_{top} - \theta_{bottom}}{z_{top} - z_{bottom}} \quad (1)$$

where θ_{top} and θ_{bottom} are the mean wind direction at heights $z_{top} = 250$ m and $z_{bottom} = 10$ m, respectively, to obtain wind directions representative of the rotor span. While the datasets yield different gradients for veer and backing, for comparability, the estimates for veer gradients were applied for the load cases with backing. Moreover, a constant gradient was assumed.



130 Although several researchers have shown that the power law profile is not able to represent realistic wind profiles (Sathe et al., 2013; Lundquist, 2022; Murphy et al., 2020; Cheynet et al., 2024), in this work, the power law is applied for simplicity. It yields the mean wind speed as a function of height, $\bar{u}(z)$, as follows:

$$\bar{u}(z) = \bar{u}_{hub} \left(\frac{z}{z_{hub}} \right)^\alpha \quad (2)$$

The power law exponent, α , was found by fitting the power law using *Scipy*'s nonlinear least squares fit (Virtanen et al., 2020) with data points up to 500 m. Although the two turbines in question have different hub heights, for simplicity, the reference mean wind speed is taken at the hub height of the IEA 15 MW turbine. That is, $z_{hub} = 150$ m and $\bar{u}_{hub} = \bar{u}|_{z=150 \text{ m}}$.

2.2.2 Load cases

Four mean wind speeds at 150 m were selected: two below-rated wind speed (5.5 m s^{-1} , 8.5 m s^{-1}), one near rated (12.5 m s^{-1}), and one above rated (16.5 m s^{-1}). For each of the four mean wind speeds, the 99th percentile of β given \bar{u}_{hub} was chosen. The power law exponent, α , was found as the mean value conditional on $\bar{u}_{hub} (\pm 0.5 \text{ m s}^{-1})$ and $\beta (\pm 0.3^\circ \text{ m}^{-1})$. Turbulence intensity at z_{hub} was estimated based on the model by Andersen and Løvseth (2006) and described by Cheynet et al. (2024):

$$I_u = 0.087 \left[1 + 0.302 \left(\frac{\bar{u}_{hub}}{10} - 1 \right) \right] \left(\frac{z_{hub}}{10} \right)^{-0.2} \quad (3)$$

Although this formulation of turbulence intensity was developed for neutral conditions and moderate to strong wind speeds, it is assumed to be sufficient for the comparative nature of this study. Coherence was set in accordance with IEC standard 61400-1 Ed. 3 (IEC, 2005) ($a_u = 12.0$ and $b_u = 0.353\text{E-}03$; $a_v, a_w \rightarrow \infty$; $b_v, b_w = 0$). The significant wave height, H_s , and peak period, T_p , were also estimated from the NORA3 dataset at Utsira Nord. H_s was taken as the 90th percentile conditional on \bar{u}_{hub} , and T_p as the mean value conditional on H_s . The Pierson–Moskowitz spectrum (Pierson and Moskowitz, 1964) was applied for the generation of irregular waves.

The environmental load cases are summarized in Table 4, and the estimated wind directions are plotted in Fig. 3. Note that the turbulence intensity increases with wind speed while the veer gradient decreases with wind speed. For each load case, a number of different wind fields were simulated to evaluate the influence of the different wind properties. These wind fields are summarized in Table 5.

One-hour simulations were considered for each load case. To avoid transients, a total simulation length of 4600 s was applied, but only the final 3600 s were used in post-processing.

155 2.2.3 Turbulence model

The turbulent inflows were based on the Kaimal spectrum with the exponential coherence model (Kaimal et al., 1972) and generated using TurbSim (Jonkman, 2016). The TurbSim temporal and spatial resolution is presented in Table 6. The choice of turbulence models and coherence is known to significantly influence the main bearing fatigue estimates (Krathe et al., 2024), floater motions (Nybø et al., 2022) and tower-top loads (Nybø et al., 2021). Future studies should also combine veer and backing with other turbulence and coherence models.

Table 4. Load cases.

Load cases	Mean wind speed at 150 m [m s ⁻¹]	Turbulence intensity [-]	Shear exponent [-]	Veer/backing gradient [° m ⁻¹]	H_s [m]	T_p [s]	Number of seeds
LC1	5.5	0.044	0.14	0.23/-0.23	2.15	8.72	6
LC2	8.5	0.048	0.11	0.17/-0.17	2.58	9.00	6
LC3	12.5	0.054	0.12	0.11/-0.11	3.35	9.51	6
LC4	16.5	0.061	0.14	0.08/-0.08	4.47	10.37	6

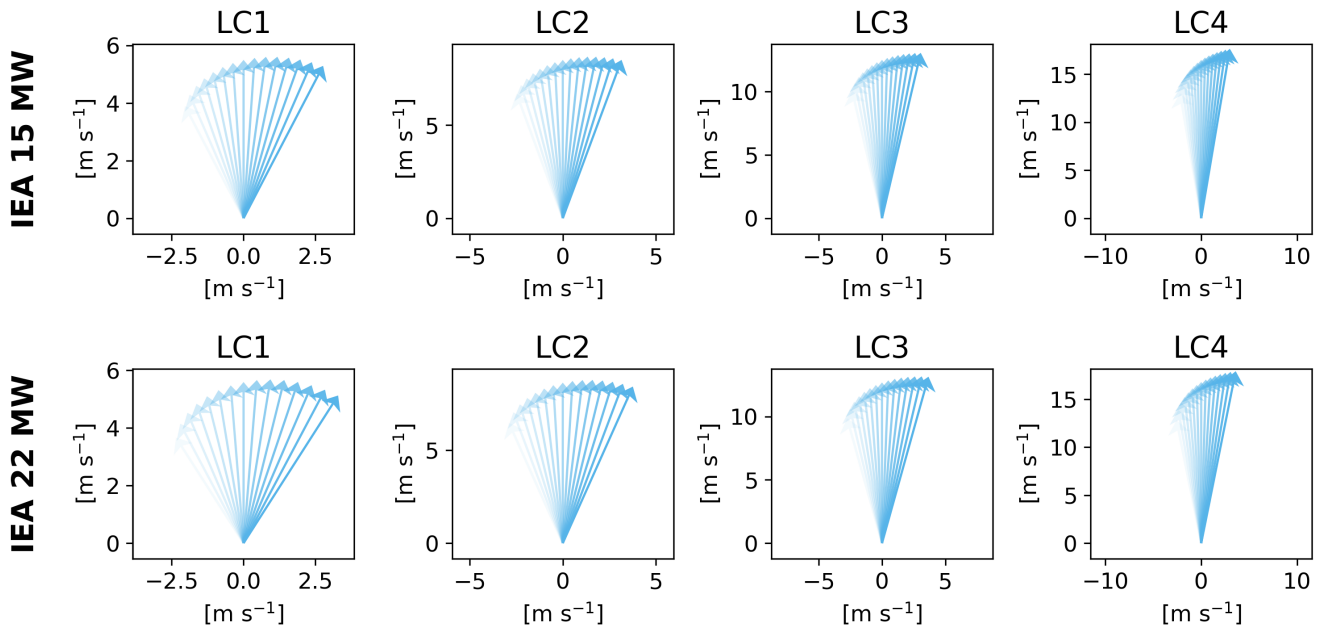


Figure 3. Mean wind vector at different heights for each load case and turbine showing changes in wind direction (veer) and mean velocity (shear) with height. The color strength increases with height.

2.3 Damage equivalent loads

2.3.1 Tower and blade damage equivalent load

Short-term DELs are calculated for each time series according to Equation 4 (Hayman, 2012) using Python scripts from the *Wind energy library* (Branlard, 2024, 2017). The load ranges, assuming zero mean and without the Goodman correction, L_i^R , are found from rainflow-counting. n_i is the number of load cycles for each load range, n^{eq} is the total number of cycles in the time series, and m is the Wöhler exponent.



Table 5. Wind fields including different properties. All conditions include waves.

Label	U	V	B	SV	ST	SVT	SBT
Description	Uniform wind	Veer	Backing	Shear and veer	Shear and turbulence	Shear, veer and turbulence	Shear, backing and turbulence

Table 6. TurbSim numerical setup.

Turbine	Δt [s]	Δy [m]	Δz [m]	Δx [m] (LC1, LC2, LC3, LC4)	Grid width [m]	Grid height [m]
IEA 15 MW	0.05	4	4.24	0.275, 0.425, 0.625, 0.825	264	280
IEA 22 MW	0.05	4	4.10	0.275, 0.425, 0.625, 0.825	316	324

$$DEL = \left(\frac{\sum_i (n_i (L_i^R)^m)}{n^{eq}} \right)^{\frac{1}{m}} \quad (4)$$

The DEL has a constant amplitude and frequency, f^{eq} , in hertz, and produces the same short-term fatigue damage, D , as the variable loads (Hayman, 2012):

$$D = \sum_i \frac{n_i}{N_i} = \frac{n^{eq}}{N^{eq}}, \quad n^{eq} = f^{eq} T \quad (5)$$

where T is the length of the time series in seconds, N^{eq} is the equivalent number of load cycles until failure, and N_i and n_i are the i th cycles to failure and number of load cycles for a time series, respectively. Here, an equivalent frequency, f^{eq} , of 1 Hz is applied. The load ranges are divided into 100 bins. The Wöhler exponent is taken as 10 for the blades and 4 for the tower. The latter choice was a compromise based on an investigation of tower stress cycles from the analyses, showing stress cycles distributed on both sides of the transition point of the bilinear SN-curve ($m = 3$ and $m = 5$).

2.3.2 Main bearing damage-equivalent loads

For the main bearings, the DEL formulation differs from that of the tower and blades. First, the dynamic equivalent radial load, P , is calculated:

$$P = XF_r + YF_a \quad (6)$$

Here, $F_r = \sqrt{F_y^2 + F_z^2}$ and $F_a = F_x$ are the time series of the radial and axial bearing loads. Only the downwind locating bearing experiences axial loads; hence, for the upwind bearing, $P = F_r$. X and Y are radial and axial load factors, depending on the ratio between axial and radial loads, $\frac{F_a}{F_r}$. These factors were estimated based on product catalogs from two bearing manufacturers (Koyo; NSK), as described by Krathe et al. (2025b), and are listed in Table 7.



Table 7. Main bearing dynamic load factors.

	$\frac{F_a}{F_r} \leq e$		$\frac{F_a}{F_r} > e$		
	X	Y	X	Y	e
MB1 (SRB, non-locating)	1	NA	NA	NA	NA
MB2 (SRB, locating)	1	4.3	0.67	6.4	0.16

For each time step, i , the equivalent radial load, P_i , is calculated and combined with the shaft speed, n_i , and the duration of
 185 each time step, t_i , to form the short-term DELs of the roller bearings (Budynas et al., 2011):

$$DEL_{MB} = \left(\frac{\sum_i^{N_t} n_i t_i P_i^{10/3}}{\sum_i^{N_t} n_i t_i} \right)^{3/10} \quad (7)$$

3 Results and discussion

3.1 Modal analysis

Tower and rotor modes were found through modal analysis by linearizing the standstill turbine in OpenFAST using the Au-
 190 tomated Campbell Diagram Code (ACDC) (Slaughter, 2024). Aerodynamics were omitted and mooring lines were replaced
 by linear springs to facilitate detection of modes. Rigid-body mode natural frequencies were found through decay tests. The
 results are summarized in Table 8 for the two turbines with rigid and flexible drivetrains. For the IEA 15 MW turbine, the tower
 natural frequencies are reduced by 2.2 % and 3.5 % when including the flexible drivetrain. Similarly, the natural frequencies of
 the asymmetric blade flap mode with pitch and blade flap with yaw are reduced by 2.2 % and 3.5 %. Considering the IEA 22
 195 MW turbine, the tower mode natural frequencies are reduced by 7–9 % with the flexible drivetrain, and the natural frequencies
 of the first asymmetric blade flap with pitch and yaw are reduced by 9 % and 12.5 %, respectively. Notably, for the 22-MW,
 the blade flap with yaw natural frequency (0.32 Hz) falls within the 3P (blade passing frequency) regime (0.35 Hz at rated
 wind speed). It is, however, important to recognize that the rotational speed will influence the natural frequencies of the rotor
 asymmetric rotor modes (typically one will increase and one will decrease with rotational speed) (Holierhoek, 2022).



Table 8. Damped natural frequencies (Hz) of the standstill floating IEA 15 MW and 22 MW turbines. The rigid body modes are the same across drivetrain models.

Mode	Description	IEA 15 MW natural frequencies [Hz]		IEA 22 MW natural frequencies [Hz]	
		Rigid drivetrain	Flexible drivetrain	Rigid drivetrain	Flexible drivetrain
		model	model	model	model
1	Platform surge		0.007		0.009
2	Platform sway		0.007		0.009
3	Platform yaw		0.011		0.011
4	Platform pitch		0.036		0.038
5	Platform roll		0.036		0.038
6	Platform heave		0.049		0.055
7	1st tower fore-aft	0.461	0.445	0.289	0.269
8	1st tower side-side	0.464	0.454	0.296	0.270
9	1st asymmetric blade flap with pitch	0.545	0.533	0.399	0.364
10	1st asymmetric blade flap with yaw	0.514	0.496	0.366	0.320
11	1st collective blade flap	0.603	0.597	0.421	0.416
12	1st collective blade edge	0.696	0.688	0.512	0.503

200 3.2 Sensitivity to drivetrain flexibility

3.2.1 Rigid and flexible drivetrain

A comparison of DELs extracted from simulations of the flexible and rigid drivetrain models are presented in Fig. 4 for each turbine. Only the SVT (shear, veer and turbulence) wind fields are considered, with one seed. The differences are compared as follows:

$$205 \quad Diff = \frac{DEL_{Flexible} - DEL_{Rigid}}{DEL_{Rigid}} \times 100 \% \quad (8)$$

Based on these simulations, it is clear that the flexibility of the drivetrain influences global response, and the effect is much more significant for the 22 MW turbine. For the tower-top fore-aft bending moment (M_y) and the torsional moment (M_z), the flexible drivetrain reduces the DELs by up to 6.5 % for the 15 MW turbine. The same responses are reduced by up to 22 % for the 22 MW with a flexible drivetrain. The differences are most significant at near- and above-rated wind speed. Note that the tower-base and tower-top torsional moments are equal. The blade-root flapwise damage-equivalent moments are reduced by a maximum of 1.5 % for the 15 MW turbine, and by a maximum of 6 % for the 22 MW turbine, but increase by 1.3 % near rated wind speed for the latter.



For the tower-base fore-aft bending moment, the effect is generally small, except at 8.5 m s^{-1} for the 22 MW turbine, where the flexible drivetrain increases DELs by 9 %. The first tower natural frequencies of the IEA 22 MW turbine fall within the 3P region. At 8.5 m s^{-1} , the tower natural frequency is close to the 3P frequency (0.26 Hz) and is shifted even closer when the flexible drivetrain is included. This could explain the increase in tower-base fore-aft bending moment DEL with flexible drivetrain in LC2. Ideally, the tower should be designed so that its natural frequencies are outside of the 3P region.

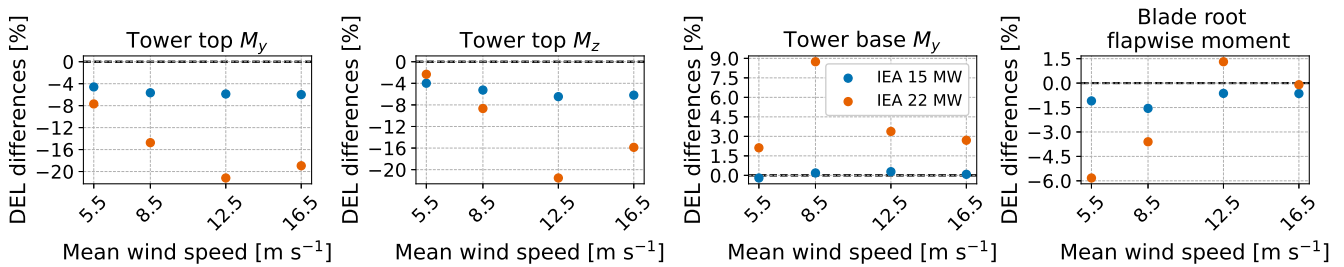


Figure 4. Tower and blade damage-equivalent moments of the flexible drivetrain model compared to the rigid drivetrain model for the IEA 15 MW and IEA 22 MW reference turbines. M_y and M_z are the fore-aft bending moment and torsional moment, respectively.

It is difficult to compare main bearing loads between the rigid and flexible drivetrain model because the rigid drivetrain model cannot output bearing loads directly. Analytical calculations could be applied, but they are complex to derive for bearings with coupling terms in their stiffness matrices. As a proxy for main bearing loads, the standard deviations of the shaft axial load and the pitch and bending moments are compared among the two models and presented in Fig. 5, calculated in similar manners as the differences in DELs. Shaft axial load standard deviations increase while shaft bending moment standard deviations are reduced with the flexible drivetrain model. Again, the most significant impact of drivetrain flexibility is seen for the 22 MW turbine, whereas the 15 MW turbine is less affected. The greatest difference in axial load standard deviations is seen for the largest wind speed and for LC2 when considering bending moments.

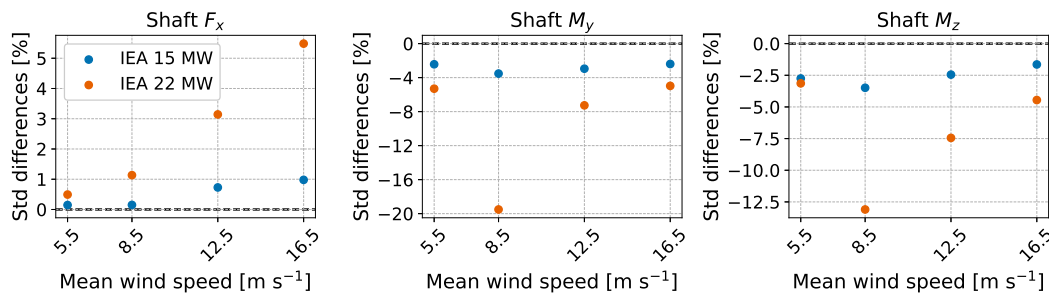


Figure 5. Differences in shaft load standard deviations among the rigid and flexible drivetrain models. F_x , M_y and M_z denote the shaft axial force, pitch moment and yaw moment, respectively.

While drivetrain flexibility significantly influences the structural response, especially for the 22 MW turbine, it does not change the mean power output of the turbines. However, the standard deviations of the power outputs are increased by up to 2.5 %.

3.2.2 Sensitivity to bearing stiffness

230 There are large uncertainties in the main bearing stiffness estimates. A test with one seed of the SVT wind fields was performed to evaluate effects of variations in bearing stiffness: in addition to the medium bearing stiffness, simulations were run with the low and high spring stiffness coefficients presented in Table 2. The differences in the tower and blade-root DELs are presented in Fig. 6. The DEL differences are calculated as

$$Diff_{Low} = \frac{DEL_{Low\ stiffness} - DEL_{Medium\ stiffness}}{DEL_{Medium\ stiffness}} \times 100\ \% \quad (9)$$

235 for the drivetrain model with low main bearing stiffness, and similarly for the model with high main bearing stiffness (replacing "Low" with "High").

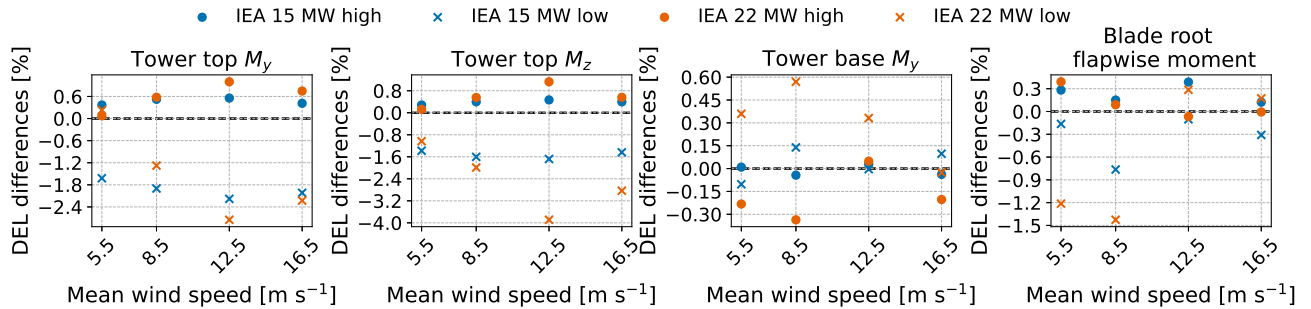


Figure 6. Tower and blade damage-equivalent moments for the IEA 15 MW and IEA 22 MW reference turbines with varying main bearing stiffness. M_y and M_z are the fore-aft bending moment and torsional moment, respectively.

This span of variation in main bearing stiffness leads to a maximum of 1.5 % difference in blade-root DELs and 0.6 % difference in tower-base DELs. Main bearing DELs (not plotted) are even less affected, with a maximum difference of 0.3 %.

240 With regard to tower-top moments, larger differences are seen, especially with reduced bearing stiffness. Low main bearing stiffness reduces the damage-equivalent fore-aft bending moment of the 15 MW turbine by up to 2.2 % and by up to 2.8 % for the 22 MW turbine. For the torsional moment DEL of the 15 MW turbine, less than 2 % reduction is seen with low bearing stiffness, whereas for the 22 MW turbine, the same DEL is reduced by 4 % for LC3. Higher main bearing stiffness leads to small increases in DELs of up to 1 %.

245 Differences in downwind main bearing radial and axial load standard deviations are plotted in Fig. 7, calculated in the same manner as the differences in DELs. Reducing the bearing stiffnesses leads to a reduction in radial load standard deviations of about 2 % for both turbines. Increasing the bearing stiffness is again less impactful, with a maximum increase in radial load



standard deviations of about 0.9 %. Axial load standard deviations generally show low sensitivity to main bearing stiffness, with maximum 1.2 % increase with reduced bearing stiffness for the 22 MW turbine. Similar results were seen for the upwind main bearing radial loads.

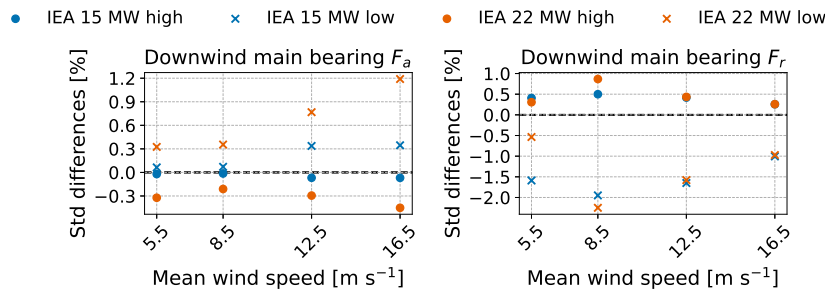


Figure 7. Downwind main bearing axial (F_a) and radial (F_r) load standard deviations of the IEA 15 MW and IEA 22 MW reference turbines with varying main bearing stiffness. The upwind main bearing radial loads showed similar trends.

250 3.3 Response to different wind fields

Because veer and backing are not mentioned in design standards, it is interesting to evaluate the importance of veer compared to the typical design case with shear and turbulence. In this section, the influence of veer and backing – relative to shear and turbulence – on different load responses is investigated. Here, the results of the wind fields SVT (shear, veer and turbulence), SBT (shear, backing and turbulence), SV (shear and veer), and ST (shear and turbulence) are compared. All conditions include waves.

3.3.1 Tower and blade DELs

DELs for the tower-top fore-aft bending moment and torsional moment, and the tower-base fore-aft bending moment are presented in Fig. 8 for wind fields SV, ST, SVT and SBT. Compared to variations between wind fields, variations among seeds were generally small.

260 Considering tower-top DELs, veer is more important than turbulence for both turbines in below-rated wind speeds, evident from the fact that both SV and SVT DELs are larger than ST DELs. For the 22 MW turbine in these conditions, veer leads to a doubling of the tower-top fore-aft DEL and an increase of more than 3 times the tower-top torsional DEL than without veer. In near-rated conditions (12.5 m s⁻¹), SVT also leads to larger DELs than ST, but this changes in above-rated wind speed, where the ST wind fields lead to slightly higher DELs than the SVT wind fields.

265 The wind fields with backing generate significantly lower tower-top DELs compared to those with veer in below-rated wind speeds. This is seen for both turbines, and the differences are again especially significant for tower-top torsional moment. However, in LC1, adding backing leads to larger DELs for the 15 MW turbine but not for the 22 MW turbine. In LC4, SBT leads to larger tower-top moment DELs than ST (up to 10 % increase for torsional moment DELs).



The differences among the wind field conditions are small for the tower-base fore-aft bending moment DEL of the 15 MW turbine, while the tower base of the 22 MW experiences a 20 % increase in fore-aft damage-equivalent bending moment in LC2 (8.5 m s^{-1}) when veer is added.

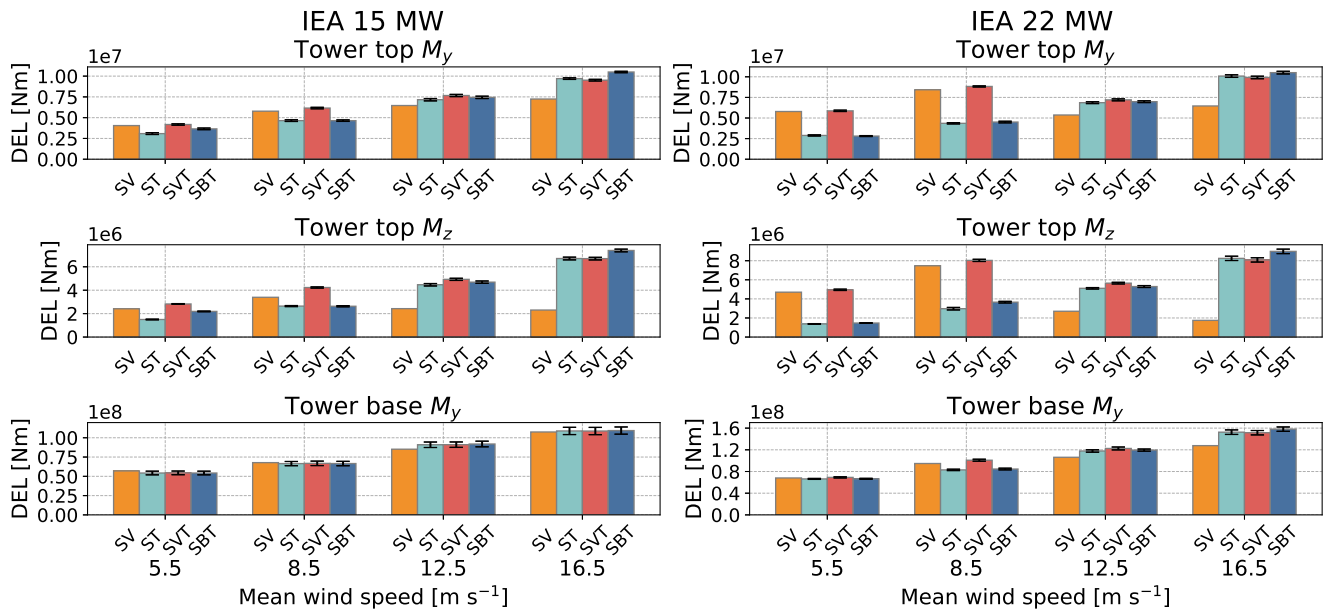


Figure 8. Tower moment DELs for the wind fields SV, ST, SVT and SBT from the flexible drivetrain model of the IEA 15 MW and IEA 22 MW reference turbines. The colored bars and the black error bars represent the mean values and standard deviations across the seeds of the turbulent wind fields, respectively. M_y and M_z are the fore-aft bending moment and torsional moment, respectively.

Blade-root flapwise damage-equivalent moments are plotted in Fig. 9. Here, veer and backing have less influence on the DELs (less than 6 % difference), except at 5.5 m s^{-1} for the 22 MW turbine, in which the inclusion of veer leads to 15 % increase in flapwise DELs.

275 3.3.2 Main bearing DELs

Main bearing DELs are presented in Fig. 10. The differences between the turbulent wind fields are small for the 15 MW turbine, less than 2.5 %. With the inclusion of veer, an increase of up to 6 % is seen for the upwind main bearing of the 22 MW turbine at 8.5 m s^{-1} mean wind speed. For the below-rated conditions, turbulence is of secondary importance, as SV and SVT give similar DELs.

280 3.3.3 Main bearing radial load standard deviations

Main bearing radial load standard deviations are also presented, see Fig. 11. Main bearing radial loads are mainly governed by shaft pitch and yaw moment, and the results are similar to those presented for the tower-top DELs. Below rated wind speed,

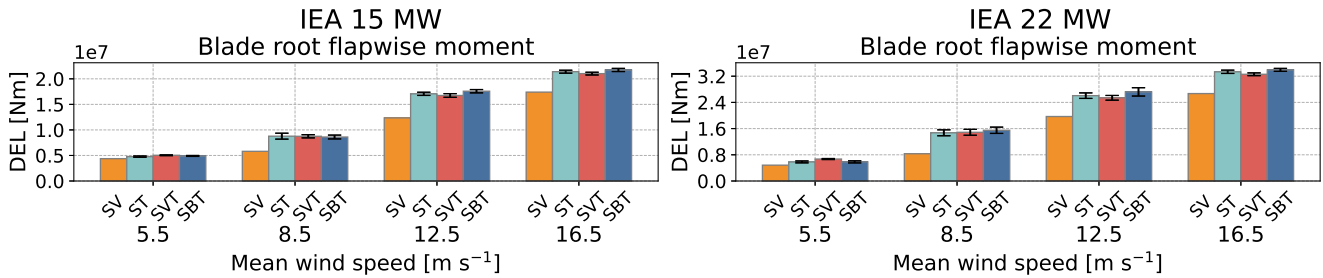


Figure 9. Blade-root flapwise DELs for the wind fields SV, ST, SVT and SBT for the flexible drivetrain model of the IEA 15 MW and IEA 22 MW turbines. The colored bars and the black error bars represent the mean values and standard deviations across the seeds of the turbulent wind fields, respectively.

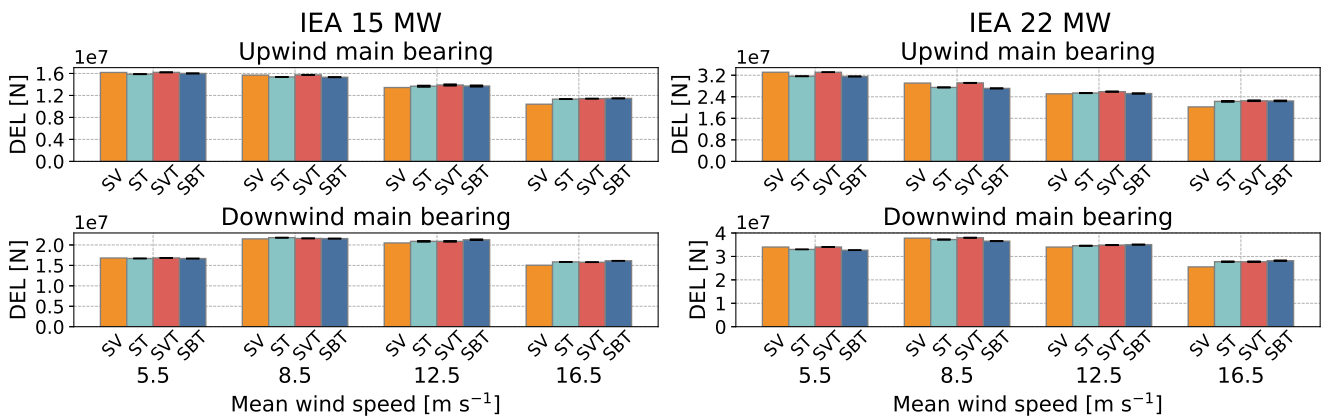


Figure 10. Main bearing DELs for the wind fields SV, ST, SVT and SBT for the flexible drivetrain model of the IEA 15 MW and IEA 22 MW turbines. The colored bars and the black error bars represent the mean values and standard deviations across the seeds of the turbulent wind fields, respectively.

veer seems to be very important. This effect is reduced with higher wind speed (and reduced veer gradient) where turbulence prevails. Hart et al. (2022) found that the influence of veer on main bearing radial load fluctuations significantly increased with turbine size. Here, the same is evident in below-rated wind speeds, where veer is generating a doubling of DELs for the 22 MW turbine and 40 % increase for the 15 MW turbine. Comparing backing and veer in below-rated conditions, they also align with those of Hart et al. (2022), who looked at veer at 10 m s^{-1} wind speed (for a wind turbine with 11.4 m s^{-1} rated wind speed) and found that veering wind led to higher main bearing radial load fluctuations than backing.

3.3.4 Response spectra

Power spectral densities of the tower-top fore-aft bending moment and blade-root flapwise moment are presented in Figs. 12–15 for wind fields ST, SBT and SVT. Similar plots for other responses can be found in Appendix A1. The spectra were calculated

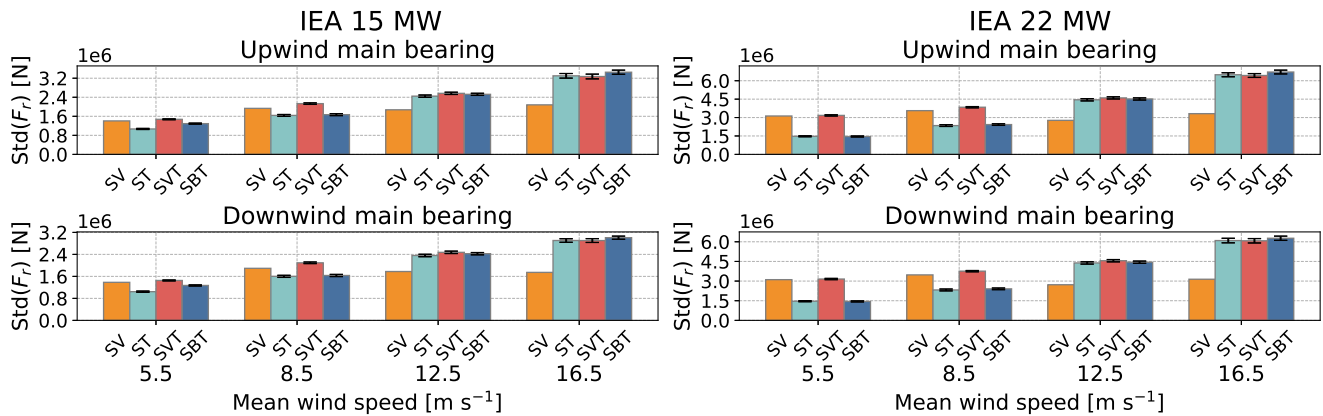


Figure 11. Main bearing radial load standard deviations for the wind fields SV, ST, SVT and SBT for the flexible drivetrain model of the IEA 15 MW and IEA 22 MW turbines. The colored bars and the black error bars represent the mean values and standard deviations (of the standard deviations) across the seeds of the turbulent wind fields, respectively.

by means of Welch’s method with Hamming window using six segments and 50 % overlap, and averaged across seeds. For both turbines, LC2 (8.5 m s^{-1}) covers an operational area with a varying rotor speed. Hence, for this load case, the 3P peak is wider than for the other load cases.

295 For the tower-top fore-aft bending moment, the peak at 3P is significantly amplified by the addition of veer in below-rated conditions. For the wind field with backing, the peak is generally comparable to the wind field without directional shear (ST), except for LC1 for the 15 MW turbine, where backing leads to a higher peak (but lower than SVT). The effect of veer is less significant near rated wind speed (LC3), and above rated, the 3P peak is lower for SVT than for ST, and the SBT peak dominates. In above-rated conditions, the 3P peak is more significant (relative to wind and waves) for the 15 MW turbine than
 300 for the 22 MW turbine. Similar trends were found for the tower-top torsional moment and the main bearing radial loads.

With regard to the blade-root flapwise moments, 1P dominates in above-rated conditions, with little difference between wind fields and turbines, although the peaks are slightly higher for SBT and ST than for SVT. Below rated, LC2 shows quite similar results for the two turbines: 2P is excited by the SVT wind field but not much by the ST and SBT wind fields, while 1P is more excited by ST and SBT than by SVT. This is also consistent with LC1. However, for LC1, the 22 MW turbine is governed
 305 by 2P (and the low-frequency turbulence) while the 15 MW turbine is dominated by 1P. The 1P excitation is well understood and driven by several characteristics of the turbulent wind field, including vertical shear, coherent eddies, tower shadow, and seemingly also wind directional shear. In contrast, the 2P excitation seems to be predominantly governed by directional shear, particularly veer. The increased significance of 2P for the 22-MW compared to the 15-MW may be attributed to its larger rotor diameter, which samples a broader range of wind directions. As a result, the 22-MW is more affected by veer—especially in
 310 LC1, which exhibits the strongest veer gradient among the load cases.

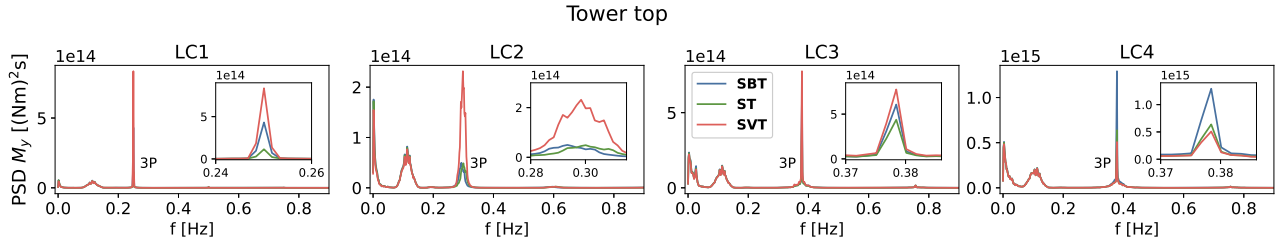


Figure 12. Power spectral densities of the IEA 15 MW turbine tower-top fore-aft bending moment for the wind fields SBT, SVT and ST. The insets show the 3P frequency. Note the variations in the x -axes of the insets.

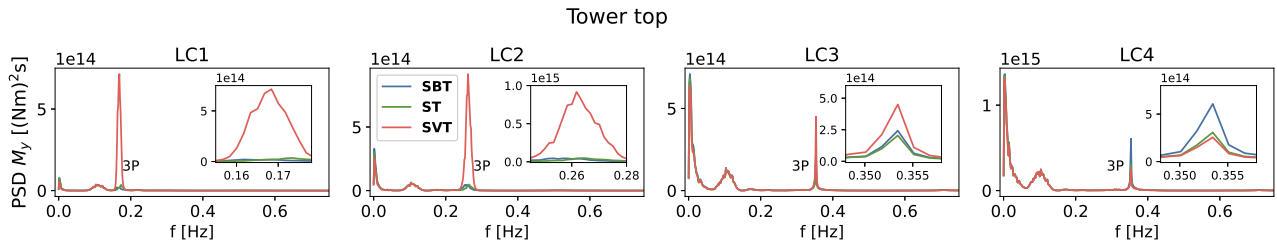


Figure 13. Power spectral densities of the IEA 22 MW turbine tower-top fore-aft bending moment for the wind fields SBT, SVT and ST. The insets show the 3P frequency. Note the variations in the x -axes of the insets.

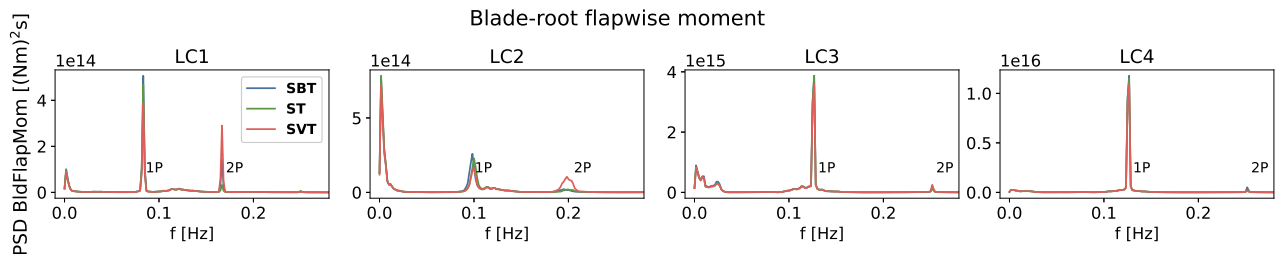


Figure 14. Power spectral densities of the IEA 15 MW turbine blade-root flapwise moment for the wind fields SBT, SVT and ST.

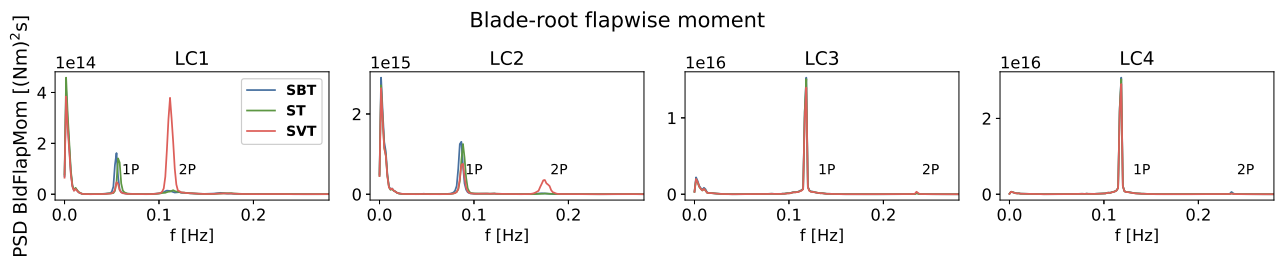


Figure 15. Power spectral densities of the IEA 22 MW turbine blade-root flapwise moment for the wind fields ST, SBT and SVT.



3.3.5 Blade-root out-of-plane bending moment in backing and veering wind

Wagner et al. (2010) illustrated how the angle of attack and relative wind speed seen by the airfoil changes with the azimuth position of a rotor blade. For a simple rotor at 8 m s^{-1} without blade pitch, for veering wind, they found that the angle of attack was larger than for uniform wind while the relative wind speed was lower. The opposite was true for backing. These combinations of angle of attack and relative wind speed led to larger amplitudes in the oscillations of the lift force for veer compared to backing. A similar study is presented in Fig. 16 for wind fields without turbulence for the 15 MW turbine: "U" (uniform wind), "B" (backing, no shear or turbulence) and "V" (veer, no shear or turbulence). These simulations were run without waves and controller, with constant blade pitch and rotor speed, and with rigid blades. The load cases with 8.5 m s^{-1} and 16.5 m s^{-1} mean wind speed at hub height were considered (LC2 and LC4, respectively). In LC2, the average blade pitch was zero, and in LC4, the blade pitch was 13.5° .

For LC2, the same effect that Wagner et al. (2010) described is seen: For backing, the angle of attack is smaller and the relative wind velocity is larger, while the opposite is true for veering wind. Angle of attack and relative wind speed seem to cancel each other in the backing case and amplify each other in the veering case. This leads to larger variations in the blade out-of-plane (OOP) bending moment in veer compared to backing. Moreover, the curves of the aerodynamic blade load (F_x) and the OOP bending moment look similar. This indicates that differences in aerodynamic loads are the primary source of differences between the wind fields, while adding gravitation and inertia loads (as in the OOP bending moment) does not change the curves much. This observation can explain the difference in the 3P peak in the response spectra of main bearing radial loads and tower-top bending moments when comparing backing and veer, and it can further explain the differences in DEL. The importance of 2P with veer can be explained by the two peaks in OOP bending moment throughout one shaft rotation, at azimuth angles of about 80° and 250° in the yellow curve ("V") in Figure 16.

In LC4, differences in angle of attack between cases are not as pronounced, whereas differences in relative wind speed are quite similar to LC2. At the same time, the large blade pitch angle of LC4 may reduce the importance of aerodynamic loads on OOP bending moment relative to gravitational and inertia loads. However, as the blade has a 13° pitch angle, it is not straightforward to compare the aerodynamic load (F_x) and the OOP bending moment for this load case.

4 Conclusions

In this work, two large floating reference wind turbines were considered. Each turbine was modeled in the coupled aero-hydro-servo-elastic simulation tool OpenFAST, including a flexible drivetrain model, incorporating drivetrain-bending degrees of freedom. These models were applied for two research purposes: First, the impact of drivetrain flexibility on global response was assessed. Second, the influence of wind directional change with height (veer and backing) on the global and main bearing DELs was investigated.

The results presented here are obtained within a set of limitations and premises. First, with rotor spans of 240 m and more, blade-bending and torsional flexibility become important. This could be more appropriately represented by the OpenFAST BeamDyn module compared to ElastoDyn. Issues related to computational efficiency prevented these simulations from being

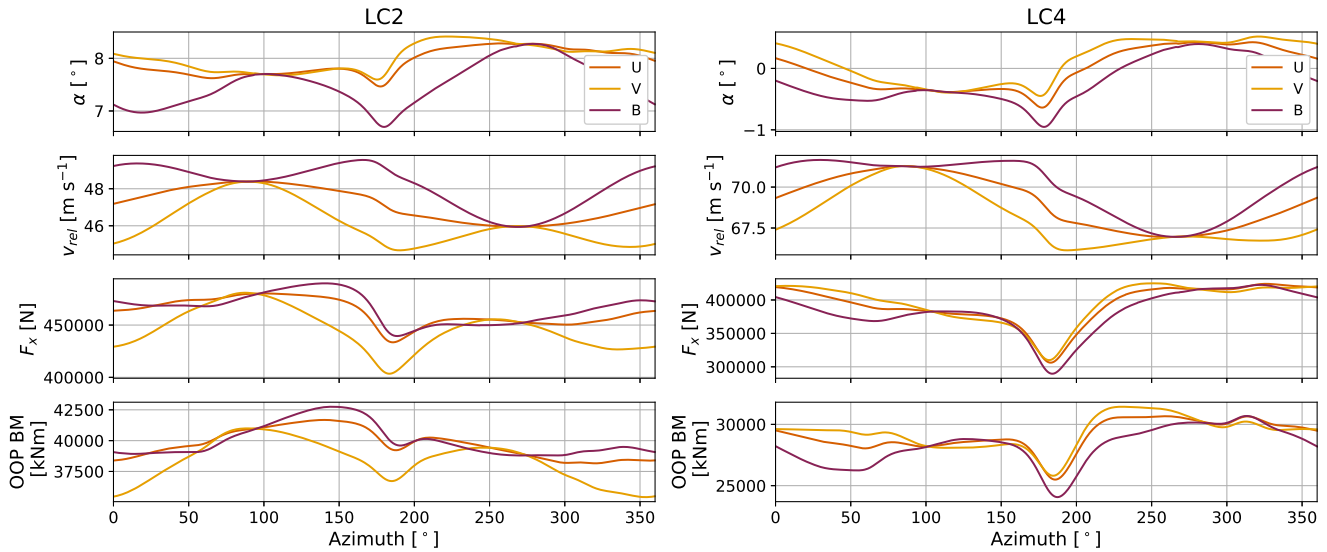


Figure 16. Blade-root out-of-plane bending moment (OOP BM) and total aerodynamic load on the blade in the flapwise direction (F_x) of the IEA 15 MW turbine plotted against rotor azimuth angle together with angle of attack (α) and the relative wind velocity (v_{rel}) that the blade sees at 75 % of its span. The blade is at its top position when the azimuth angle is $0/360^\circ$ and passes the tower at 180° . Note that the blade pitch angle is 13.5° (toward feathered) for LC4 and 0° for LC2. Note also that the aerodynamic load (F_x) is in a coordinate system that pitches with the blade (F_x points into the rotor plane when the blade pitch is 0°).

performed with BeamDyn. However, future work – aided by the upcoming upgrade to OpenFAST with tight coupling that will
 345 greatly speed up simulations with BeamDyn enabled – should investigate the interplay between blade flexibility and veer loading,
 ing, and between blade flexibility and drivetrain flexibility. Second, there are large uncertainties with estimating main bearing
 stiffness coefficients of large main bearings, as these are not readily available from manufacturers. An attempt to account for
 this uncertainty was made by considering a span of main bearing stiffnesses. Finally, with regard to environmental conditions,
 a constant veer gradient throughout the rotor plane was considered while other nonlinear variations of wind direction with
 350 height were also observed in the dataset. Similarly, a power law shear profile was assumed, although the dataset showed that
 some wind profiles associated with high veer are not well represented by the power law. Moreover, TurbSim was applied for
 generating synthetic turbulence; research has shown that different turbulence generators yield different fatigue loads.

The turbines with flexible drivetrains exhibit lower tower and rotor natural frequencies. The first tower natural frequencies
 are reduced by 2–3.5 % for the 15 MW turbine and by 7–9 % for the 22 MW turbine compared to models with rigid drivetrains.
 355 Similarly, natural frequencies of the asymmetric blade flap with pitch and blade flap with yaw modes (for a standstill turbine
 without aerodynamics) are reduced by 2 % and 3.5 % for the 15 MW turbine and by 9 % and 12.5 % for the 22 MW turbine.
 The asymmetric blade flap with yaw mode falls within the 3P regime of the 22 MW turbine, but this finding is for a standstill
 turbine, and frequencies may change with wind and rotor speeds and aerodynamic loads.



Including the flexible drivetrain in the global analysis leads to significant reductions in tower-top torsional and fore-aft
360 damage-equivalent bending moment, especially for the 22 MW turbine (22 %), but also for the 15 MW turbine (6.5 %). Blade-
root flapwise damage-equivalent moments are less influenced, but show reductions of up to 6 % for the 22 MW turbine and
1.5 % for the 15 MW turbine. The tower-base fore-aft damage equivalent bending moment is generally little affected by the
flexible drivetrain, except at 8.5 m s^{-1} , where it leads to 9 % increase in DEL for the 22 MW. This is likely because the floating
tower natural frequency of the IEA 22 MW turbine falls within the 3P region (and more so with a flexible drivetrain), which is
365 not an optimal design.

For the second objective, four sets of load cases were defined, two with mean wind speeds below rated, one near (slightly
above) rated and one above rated wind speed. Environmental data were estimated from NORA3 data (Haakenstad et al., 2021;
Cheynet et al., 2023, 2024) at Utsira Nord, a location intended for floating wind farms off the coast of Norway. For each load
case, a set of seven wind fields were defined: 1) uniform constant wind, 2) wind with a veer profile, 3) wind with a backing
370 profile, 4) wind with a shear and veer profile, 5) wind with shear and turbulence, 6) wind with shear, veer and turbulence, and
7) wind with shear, backing and turbulence. All conditions included waves. Coupled simulations were run for each turbine and
each wind field within each load case. DELs of the tower fore-aft bending moment and torsional moment, blade-root flapwise
moment and main bearings were investigated.

When comparing turbulent wind fields with and without veer and backing, it is clear that veer becomes very important in
375 some load cases. For the lowest wind speed (and highest veer gradient), the tower-top DELs are underestimated by 50 %
(fore-aft bending moment) and 72 % (torsional moment) for the 22 MW turbine when omitting veer. For the 15 MW turbine,
the corresponding underestimations are 25 % and 47 %. Backing also leads to increased DELs for the 15 MW at the lowest
wind speed (5.5 m s^{-1} , 16 % for the fore-aft bending moment, 32 % for the torsional moment), but has low effect on the DELs
of the 22 MW turbine in the same load case. With increasing wind speed (and lower veer gradient and increasing turbulence
380 intensity), veer becomes less important. Similar trends are found for the main bearing radial load standard deviations, while
main bearing DELs exhibit little impact of veer and backing. Blade-root damage-equivalent moments are also less affected,
with an exception of a 15 % increase in DELs at 5.5 m s^{-1} mean wind speed for the 22 MW turbine when including veer.

Looking at the response spectra, 3P (not surprisingly) is identified as the major driver of the differences in tower DELs while
1P and 2P frequencies govern the blade-root flapwise DELs. The 2P peak is significantly larger for the wind fields including
385 veer than those with backing in below-rated wind speeds. The combination of changes in relative velocity and angle of attack
are thought to cause these differences between backing and veer.

To summarize, veer can be of very high importance to DELs, depending on turbine size, veer gradient and operating regime.
Moreover, including drivetrain flexibility in global analyses significantly reduces the tower-top DELs, especially for the largest
turbine. Recommendations for future work include investigating the influence of low-level jets and other shear profiles on the
390 main bearing and tower-top response, preferably together with wind directional shear (veer and backing), and investigating the
effects of combining higher fidelity blade models with flexible drivetrains in global analyses.



Code availability. Code applied to build OpenFAST drivetrain models is open access (Krathe, 2024).

Appendix A: Response spectra

A1 Turbulent, sheared wind with and without veer

395 A1.1 IEA 15 MW turbine

Figures A1–A3 present power spectral densities of the tower-top torsional moment, tower-base fore-aft bending moment and upwind main bearing radial loads of the IEA 15 MW turbine subjected to turbulent, sheared wind with and without veer.

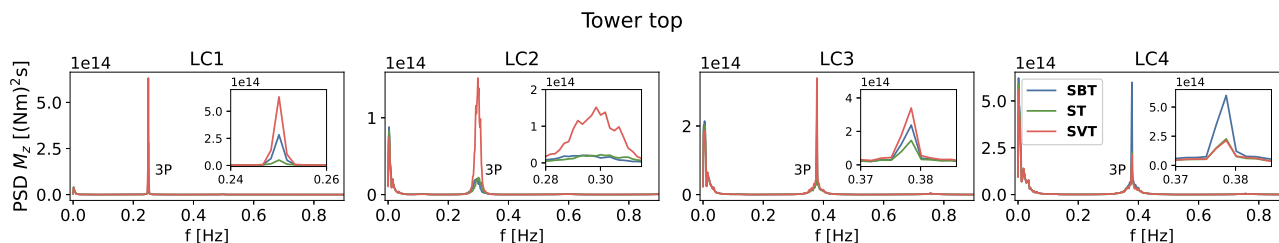


Figure A1. Power spectral densities of the IEA 15 MW turbine tower-top torsional moment for the wind fields ST, STB and SVT. The insets show the 3P frequency. Note the variations in the x -axes of the insets.

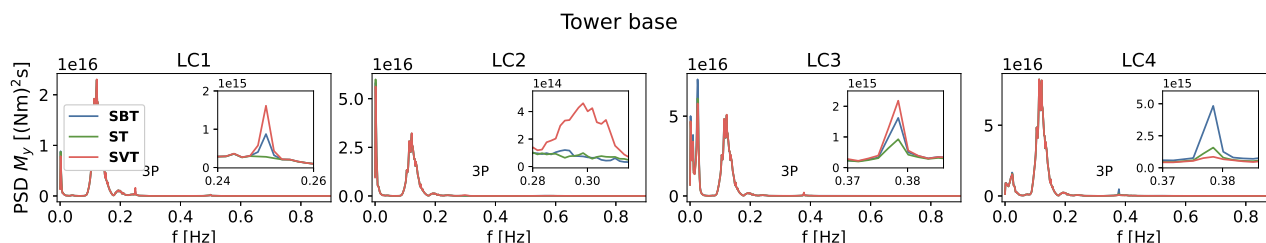


Figure A2. Power spectral densities of the IEA 15 MW turbine tower-base fore-aft bending moment for the wind fields ST, STB and SVT. The insets show the 3P frequency. Note the variations in the x -axes of the insets.

A1.2 IEA 22 MW turbine

Figure A4 and Fig. A6 present power spectral densities of the tower-top torsional moment, tower-base fore-aft bending moment and upwind main bearing radial loads of the IEA 22 MW turbine subjected to turbulent, sheared wind with and without veer.

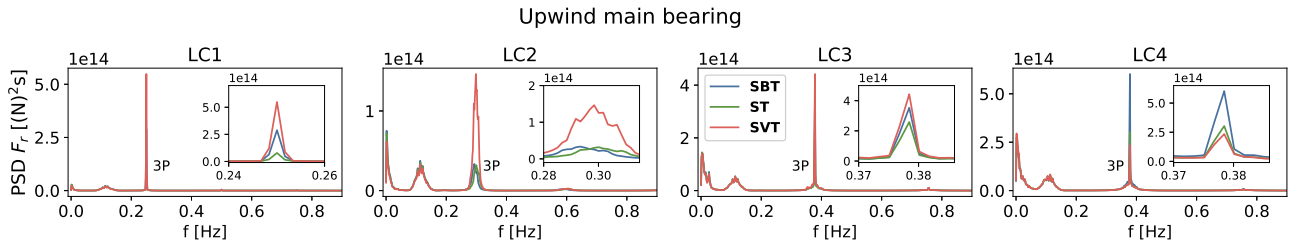


Figure A3. Power spectral densities of the IEA 15 MW turbine upwind main bearing radial load for the wind fields ST, SBT and SVT. The downwind main bearing showed similar trends. The insets show the 3P frequency. Note the variations in the x -axes of the insets.

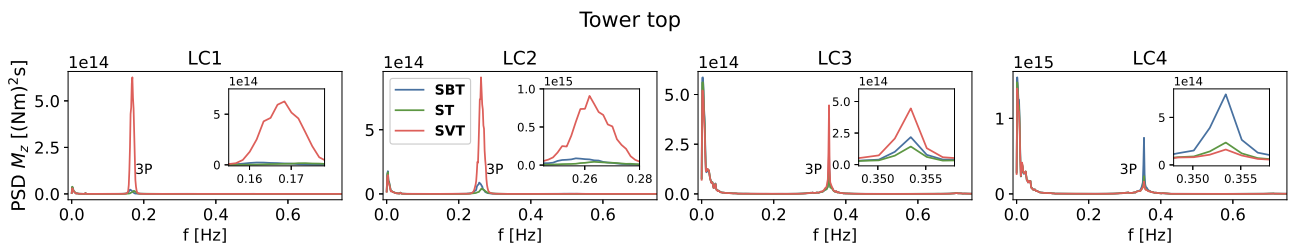


Figure A4. Power spectral densities of the IEA 22 MW turbine tower-top torsional moment for the wind fields ST, SBT and SVT. The insets show the 3P frequency. Note the variations in the x -axes of the insets.

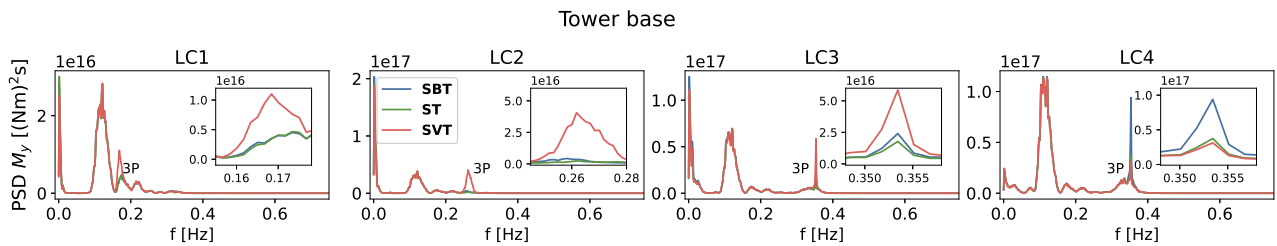


Figure A5. Power spectral densities of the IEA 22 MW turbine tower-base fore-aft bending moment for the wind fields SBT, SVT and ST. The insets show the 3P frequency. Note the variations in the x -axes of the insets.

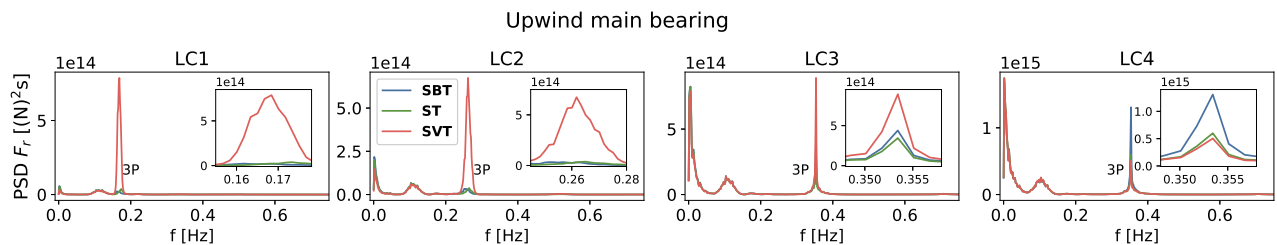


Figure A6. Power spectral densities of the IEA 22 MW turbine upwind main bearing radial load for the wind fields ST, SBT and SVT. The downwind main bearing showed similar trends. The insets show the 3P frequency. Note the variations in the x -axes of the insets.



Author contributions. Veronica Liverud Krathe built the coupled turbine models, analyzed NORA3 data to assemble the load cases, performed the analyses and the post-processing, wrote the manuscript, and did the editing of the draft and the final manuscript. Jason Jonkman and Erin Elizabeth Bachynski-Polić provided supervision, validated the results, and reviewed and edited the manuscript.

Competing interests. One of the co-authors of this paper, Erin E. Bachynski-Polić, is an associate editor of Wind Energy Science.

405 *Disclaimer.* The views expressed in the article do not necessarily represent the views of the DOE or the U.S. Government. The U.S. Government retains and the publisher, by accepting the article for publication, acknowledges that the U.S. Government retains a nonexclusive, paid-up, irrevocable, worldwide license to publish or reproduce the published form of this work, or allow others to do so, for U.S. Government purposes

410 *Acknowledgements.* The authors would like to acknowledge Rebeca Marini at VUB and Etienne Cheynet at UiB for fruitful discussions. This work is partly funded by the FME NorthWind project (grant 321954), funded by the Norwegian Research Council. This work was authored in part by the National Renewable Energy Laboratory for the U.S. Department of Energy (DOE) under Contract No. DE-AC36-08GO28308. Funding provided by the U.S. Department of Energy Office of Energy Efficiency and Renewable Energy Wind Energy Technologies Office.



References

- NEK IEC 61400-1:2005 Wind energy generation systems – Part 1: Design requirements Ed. 3, 2005.
- 415 NEK IEC 61400-1:2019 Wind energy generation systems – Part 1: Design requirements Ed. 4, 2019.
- Abbas, N. J., Zalkind, D., Mudafort, R. M., Hylander, G., Mulders, S., Heffernan, D., and Bortolotti, P.: NREL/ROSCO: ROSCO v2.9.0, <https://doi.org/10.5281/zenodo.10535404>, 2024.
- Allen, C., Viselli, A., Dagher, H., Goupee, A. J., Gaertner, E., Abbas, N., Hall, M., Barter, G., and Wind, I. E. A.: Definition of the UMaine VoltturnUS-S Reference Platform Developed for the IEA Wind 15- Megawatt Offshore Reference Wind Turbine, Tech. rep., NREL, 2020.
- 420 Andersen, O. J. and Løvseth, J.: The Frøya database and maritime boundary layer wind description, *Marine Structures*, 19, 173–192, <https://doi.org/https://doi.org/10.1016/j.marstruc.2006.07.003>, 2006.
- Bak, C., Aagaard Madsen, H., and Johansen, J.: Influence from blade-tower interaction on fatigue loads and dynamics (poster), 2001.
- Barter, G., Bortolotti, P., Gaertner, E., Rinker, J., Abbas, N. J., dzalkind, Zahle, F., T-Wainwright, Branlard, E., Wang, L., Padrón, L. A., Hall, M., and Issraman: IEAWindTask37/IEA-15-240-RWT, <https://doi.org/10.5281/zenodo.10664562>, 2024.
- 425 Bodini, N., Lundquist, J. K., and Kirincich, A.: U.S. East Coast Lidar Measurements Show Offshore Wind Turbines Will Encounter Very Low Atmospheric Turbulence, *Geophysical Research Letters*, 46, 5582–5591, <https://doi.org/10.1029/2019GL082636>, 2019.
- Bodini, N., Lundquist, J. K., and Kirincich, A.: Offshore Wind Turbines Will Encounter Very Low Atmospheric Turbulence, in: *Journal of Physics: Conference Series*, vol. 1452, Institute of Physics Publishing, ISSN 17426596, <https://doi.org/10.1088/1742-6596/1452/1/012023>, 2020.
- 430 Branlard, E.: *Wind Turbine Aerodynamics and Vorticity-Based Methods: Fundamentals and Recent Applications*, Springer International Publishing, ISBN 978-3-319-55163-0, <https://doi.org/10.1007/978-3-319-55164-7>, 2017.
- Branlard, E.: *welib: A Python Library for Wind Energy Applications*, <https://github.com/ebanlard/welib>, 2024.
- Budynas, R. G. R. G., Nisbett, J. K., and Shigley, J. E.: *Shigley’s mechanical engineering design*, McGraw-Hill, ISBN 0073529281, 2011.
- Cheyne, E., Li, L., and Jiang, Z.: Spatially averaged metocean data at Utsira Nord (UN) and Sørilige Nordsjø II (SN2) with NORA3 (1982-435 2022), <https://doi.org/10.5281/zenodo.10048159>, 2023.
- Cheyne, E., Li, L., and Jiang, Z.: Metocean conditions at two Norwegian sites for development of offshore wind farms, *Renewable Energy*, 224, 120 184, <https://doi.org/https://doi.org/10.1016/j.renene.2024.120184>, 2024.
- Gaertner, E., Rinker, J., Sethuraman, L., Zahle, F., Anderson, B., Barter, G., Abbas, N., Meng, F., Bortolotti, P., Skrzypiąski, W., Scott, G., Feil, R., Bredmose, H., Dykes, K., Shields, M., Allen, C., Viselli, A., and Wind, I. E. A.: Definition of the IEA Wind 15-Megawatt 440 Offshore Reference Wind Turbine, Tech. Rep. NREL/TP-5000-75698, NREL, 2020.
- Haakenstad, H. and Breivik, Ø.: NORA3. Part II: Precipitation and Temperature Statistics in Complex Terrain Modeled with a Nonhydrostatic Model, *Journal of Applied Meteorology and Climatology*, 61, 1549 – 1572, <https://doi.org/10.1175/JAMC-D-22-0005.1>, 2022.
- Haakenstad, H., Breivik, Ø., Furevik, B. R., Reistad, M., Bohlinger, P., and Aarnes, O. J.: NORA3: A Nonhydrostatic High-Resolution Hindcast of the North Sea, the Norwegian Sea, and the Barents Sea, *Journal of Applied Meteorology and Climatology*, 60, 1443 – 1464, 445 <https://doi.org/10.1175/JAMC-D-21-0029.1>, 2021.
- Hart, E., Stock, A., Elderfield, G., Elliott, R., Brasseur, J., Keller, J., Guo, Y., and Song, W.: Impacts of wind field characteristics and non-steady deterministic wind events on time-varying main-bearing loads, *Wind Energy Science*, 7, 1209–1226, <https://doi.org/10.5194/wes-7-1209-2022>, 2022.
- Hayman, G. J.: *MLife Theory Manual for Version 1.00*, Tech. rep., NREL, <http://www.osti.gov/bridge>, 2012.



- 450 Hersbach, H., Bell, B., Berrisford, P., Hirahara, S., Horányi, A., Muñoz-Sabater, J., Nicolas, J., Peubey, C., Radu, R., Schepers, D., Simons, A., Soci, C., Abdalla, S., Abellan, X., Balsamo, G., Bechtold, P., Biavati, G., Bidlot, J., Bonavita, M., De Chiara, G., Dahlgren, P., Dee, D., Diamantakis, M., Dragani, R., Flemming, J., Forbes, R., Fuentes, M., Geer, A., Haimberger, L., Healy, S., Hogan, R. J., Hólm, E., Janisková, M., Keeley, S., Laloyaux, P., Lopez, P., Lupu, C., Radnoti, G., de Rosnay, P., Rozum, I., Vamborg, F., Villaume, S., and Thépaut, J. N.: The ERA5 global reanalysis, *Quarterly Journal of the Royal Meteorological Society*, 146, 1999–2049, <https://doi.org/10.1002/qj.3803>, 2020.
- 455 Holierhoek, J. G.: Aeroelastic Stability Models, in: *Handbook of Wind Energy Aerodynamics*, edited by Stoevesandt, B., Schepers, G., Fuglsang, P., and Sun, Y., chap. 16, Springer, 2022.
- IRENA: *Future of Wind: Deployment, Investment, Technology, Grid Integration and Socio-Economic Aspects (A Global Energy Transformation paper)*, Tech. rep., Abu Dhabi, 2019.
- 460 Jonkman, B., Platt, A., Mudafort, R. M., Branlard, E., Sprague, M., Ross, H., Jonkman, J., Hayman, G., Slaughter, D., Hall, M., Vijayakumar, G., Buhl, M., Bortolotti, P., Ananthan, S., Davies, R., S., M., Rood, J., Damiani, R., Mendoza, R., Long, H., Schuenemann, P., Shaler, K., Housner, S., Sakievich, P., Wang, L., Bendl, K., and Carmo, L.: *OpenFAST/openfast: v3.5.2*, <https://doi.org/10.5281/zenodo.10530537>, 2024.
- Jonkman, B. J.: *TurbSim User’s Guide v2.00.00*, Tech. rep., National Renewable Energy Laboratory, 2016.
- 465 Kaimal, J. C., Wyngaard, J. C., Izumi, Y., and Coté, O. R.: Spectral characteristics of surface-layer turbulence, *Quarterly Journal of the Royal Meteorological Society*, 98, 563–589, <https://doi.org/https://doi.org/10.1002/qj.49709841707>, 1972.
- Koyo: Large size ball & roller bearings. General bearings, <https://koyo.jtekt.co.jp/en/support/catalog-download/uploads/catbs008en.pdf>.
- Krathe, V. L.: *SubDrive: OpenFAST-drivetrain-modeling*, <https://github.com/verlivkra/SubDrive>, 2024.
- Krathe, V. L., Jonkman, J., Gebel, J., Rivera-Arreba, I., Nejad, A., and Bachynski-Polić, E. E.: Investigation of main bearing fatigue estimate sensitivity to synthetic turbulence models using a novel drivetrain model implemented in OpenFAST. Preprint., <https://doi.org/10.22541/au.172514690.08137186/v1>, 2024.
- 470 Krathe, V. L., Jonkman, J., Gebel, J., Rivera-Arreba, I., Nejad, A., and Bachynski-Polić, E. E.: Investigation of Main Bearing Fatigue Estimate Sensitivity to Synthetic Turbulence Models Using a Novel Drivetrain Model Implemented in OpenFAST, *Wind Energy*, 28, e70005, <https://doi.org/https://doi.org/10.1002/we.70005>, 2025a.
- 475 Krathe, V. L., Thedin, R., Jonkman, J. M., Nejad, A. R., and Bachynski-Polić, E. E.: Main bearing response in a waked 15-MW floating wind turbine in below-rated conditions, *Forschung im Ingenieurwesen*, 89, 37, <https://doi.org/10.1007/s10010-025-00808-z>, 2025b.
- Lundquist, J. K.: Wind Shear and Wind Veer Effects on Wind Turbines, in: *Handbook of Wind Energy Aerodynamics*, edited by Stoevesandt, B., Schepers, G., Fuglsang, P., and Sun, Y., chap. 27, Springer, 2022.
- Marini, R., Vratsinis, K., Kestel, K., Sterckx, J., Matthys, J., Daems, P.-J., Verstraeten, T., and Helsen, J.: Assessing the impact of wind profiles at offshore wind farm sites for field data-enabled design (Preprint), *Wind Energ. Sci. Discuss.*, 2025, 1–32, <https://doi.org/10.5194/wes-2025-9>, 2025.
- 480 Murphy, P., Lundquist, J. K., and Fleming, P.: How wind speed shear and directional veer affect the power production of a megawatt-scale operational wind turbine, *Wind Energ. Sci.*, 5, 1169–1190, <https://doi.org/10.5194/wes-5-1169-2020>, 2020.
- NREL: *SubDyn User Guide and Theory Manual*, <https://openfast.readthedocs.io/en/main/source/user/subdyn/modeling.html#substructure-tower-turbine-coupling>, 2024.
- 485 NSK: Large size rolling bearings, <https://www.nsk-literature.com/en/large-size-rolling-bearings/offline/download.pdf>.



- Nybø, A., Nielsen, F. G., and Godvik, M.: Quasi-static response of a bottom-fixed wind turbine subject to various incident wind fields, *Wind Energy*, 24, 1482–1500, <https://doi.org/10.1002/we.2642>, 2021.
- 490 Nybø, A., Gunnar Nielsen, F., and Godvik, M.: Sensitivity of the dynamic response of a multimegawatt floating wind turbine to the choice of turbulence model, *Wind Energy*, 25, 1013–1029, <https://doi.org/https://doi.org/10.1002/we.2712>, 2022.
- Pierson, W. J. and Moskowitz, L.: A proposed spectral form for fully developed wind seas based on the similarity theory of S. A. Kitaigorodskii, *Journal of Geophysical Research*, 69, 5181–5190, <https://doi.org/10.1029/jz069i024p05181>, 1964.
- Robertson, A. N., Shaler, K., Sethuraman, L., and Jonkman, J.: Sensitivity analysis of the effect of wind characteristics and turbine properties on wind turbine loads, *Wind Energy Science*, 4, 479–513, <https://doi.org/10.5194/WES-4-479-2019>, 2019.
- 495 Royston, T. J. and Basdogan, I.: Vibration transmission through self-aligning (spherical) rolling element bearings: Theory and experiment, *Journal of Sound and Vibration*, 215, 997–1014, <https://doi.org/https://doi.org/10.1006/jsvi.1998.9999>, 1998.
- Sathe, A., Mann, J., Barlas, T., Bierbooms, W., and van Bussel, G. J. W.: Influence of atmospheric stability on wind turbine loads, *Wind Energy*, 16, 1013–1032, <https://doi.org/https://doi.org/10.1002/we.1528>, 2013.
- Schaeffler: BEARINX-online Easy Friction, <https://bearinx-online-easy-friction.schaeffler.com/>, 2025.
- 500 Shu, Z., Li, Q., He, Y., and Chan, P. W.: Investigation of marine wind veer characteristics using wind lidar measurements, *Atmosphere*, 11, <https://doi.org/10.3390/atmos11111178>, 2020.
- Slaughter, D.: OpenFAST/acdc: v0.5.0-alpha, <https://doi.org/10.5281/zenodo.11210222>, 2024.
- Stull, R. B.: Introduction to boundary layer meteorology, Kluwer Academic Publishers, 1988.
- Torsvik, J.: Dynamic Analysis in Design and Operation of Large Floating Offshore Wind Turbine Drivetrains, Ph.D. thesis, NTNU, Trondheim, 2020.
- 505 Virtanen, P., Gommers, R., Oliphant, T. E., Haberland, M., Reddy, T., Cournapeau, D., Burovski, E., Peterson, P., Weckesser, W., Bright, J., van der Walt, S. J., Brett, M., Wilson, J., Millman, K. J., Mayorov, N., Nelson, A. R. J., Jones, E., Kern, R., Larson, E., Carey, C. J., Polat, I., Feng, Y., Moore, E. W., VanderPlas, J., Laxalde, D., Perktold, J., Cimrman, R., Henriksen, I., Quintero, E. A., Harris, C. R., Archibald, A. M., Ribeiro, A. H., Pedregosa, F., van Mulbregt, P., and SciPy 1.0 Contributors: SciPy 1.0: Fundamental Algorithms for Scientific Computing in Python, *Nature Methods*, 17, 261–272, <https://doi.org/10.1038/s41592-019-0686-2>, 2020.
- Wagner, R., Courtney, M., Larsen, T. J., and Schmidt Paulsen, U.: Simulation of shear and turbulence impact on wind turbine performance, Tech. rep., Danmarks Tekniske Universitet, Risø Nationallaboratoriet for Bæredygtig Energi, Risøe, Denmark, ISBN 9788755038011, www.risoe.dtu.dk, 2010.
- Wang, S., Moan, T., and Nejad, A. R.: A comparative study of fully coupled and de-coupled methods on dynamic behaviour of floating wind turbine drivetrains, *Renewable Energy*, 179, 1618–1635, <https://doi.org/https://doi.org/10.1016/j.renene.2021.07.136>, 2021.
- 515 Wiley, W., Jonkman, J., Robertson, A., and Shaler, K.: Sensitivity analysis of numerical modeling input parameters on floating offshore wind turbine loads, *Wind Energy Science*, 8, 1575–1595, <https://doi.org/10.5194/wes-8-1575-2023>, 2023.
- Zahle, F., Barlas, A., Lønbaek, K., Bortolotti, P., Zalkind, D., Wang, L., Labuschagne, C., Sethuraman, L., and Barter, G.: Definition of the IEA Wind 22-Megawatt Offshore Reference Wind Turbine, Tech. rep., Technical University of Denmark, International Energy Agency, ISBN 978-87-87335-71-3, <https://doi.org/10.11581/DTU.00000317>, 2024a.
- 520 Zahle, F., Barlas, T., Lønbaek, K., Bortolotti, P., Zalkind, D., Wang, L., Labuschagne, C., Sethuraman, L., Barter, G., and Marten, D.: IEAWindTask37/IEA-22-280-RWT: v1.0.1, <https://doi.org/10.5281/zenodo.10944127>, 2024b.